공학석사학위논문

Effects of an Improved Engine-Nacelle Tilting Mechanism upon the Tiltrotor Aircraft Aeromechanics and Aeroelasticity

개선된 엔진-나셀 틸팅 메커니즘에 따른 틸트로터 항공기의 공기역학 및 공력탄성학 효과

2023 년 8월

서울대학교 대학원
항공우주공학과
이 현 재

Effects of an Improved Engine-Nacelle Tilting Mechanism upon the Tiltrotor Aircraft Aeromechanics and Aeroelasticity

개선된 엔진-나셀 틸팅 메커니즘에 따른 틸트로터 항공기의 공기역학 및 공력탄성학 효과

지도교수 신 상 준

이 논문을 공학석사 학위논문으로 제출함

2023 년 6 월

서울대학교 대학원
항공우주공학과
이 현 재

이현재의 공학석사 학위논문을 인준함

2023 년 6 월

위 원 장	이 관 중	(인)
부위원장	신 상 준	(인)
위 원	이 재 하	(인)

Abstract

Effects of an Improved Engine-Nacelle Tilting Mechanism upon the Tiltrotor Aircraft Aeromechanics and Aeroelasticity

Hyunjae Lee

Department of Aerospace Engineering

The Graduate School

Seoul National University

A tiltrotor aircraft provides advantages in that vertical takeoff and high cruise speed compared against the conventional helicopters. Though it is susceptible to aeroelastic instability due to the interaction between the wings and rotors at a high forward speed. Various methods have been attempted to address such issue, while including the pitch-flap coupling, flap-hinge offset, and adjustment of the stiffness and damping ratio of the engine/nacelle. However, researches considering the aeroelastic characteristics of the entire drive system of a tiltrotor aircraft has been rarely conducted.

In this thesis, an influence of the engine/nacelle drive system upon the whirl flutter of a tiltrotor aircraft is analyzed. The analysis is conducted using XV-15 aircraft as a baseline object, with the engine/nacelle drive system replaced by that of the recent

V280 Valor aircraft, which incorporates an improved tilting mechanism.

First, the gear ratio and initial configuration of the target gear assembly is determined using a top-down approach. Load analysis is then performed for the gear design to determine the required sizing condition. The quasi-steady transition analysis of XV-15 rotor is carried out by using CAMRAD II free wake aerodynamics. Based on the results, the load condition is determined employing the physics-based approach. Next, the gear and drive system sizing is performed, and the obtained results are applied to the baseline aircraft to conduct the mode shape analysis by NASTRAN. The engine-nacelle drive system is attached on the wing tip with the rigid body element, while considering its elasticity. Finally, utilizing the flutter analysis module of CAMRAD II, trim analysis is performed. To assess the influence of the improved drive-system on the aeroelasticity, the critical damping and the frequency effects are analyzed.

Keywords: Tiltrotor, Whirl flutter, Engine-nacelle rotating mechanism, Gearbox Design

Student Number: 2021-23313

Contents

List of Tables

Page

List of Figures

Page

Chapter 1

Introduction

1.1 Background and motivation

The tiltrotor aircraft serves as a solution for achieving high speed vertical lift, offering substantial improvement in terms of the range and speed. It is done while still maintaining the vertical lift capability of the conventional edgewise rotor helicopters. In a typical tiltrotor aircraft, the axis of the engine-nacelle attached to the main wing tip is parallel to the axis of the rotor hub. As a result, the drive-system of both engine-nacelle and rotor hub axis are mounted within a single housing and rotate together in parallel [1] as shown in Fig. 1. Bell V-22 Osprey, most widely operated as the first mass produced tiltrotor aircraft, along its predecessor XV-15, are the representative examples of such rotating mechanism [2].

However, a tiltrotor aircraft, due to its high cruise speed, experiences various aeroelastic instabilities. Among those, whirl flutter has been the most extensively studied. In it, the phenomenon was considered to be induced by the aerodynamic loads resulting from the precession on the propellers and nacelles, as the inflow speed through the rotor blades increased [3].

Numerous researches have been conducted to overcome the limitations on the forward speed by whirl flutter. Design variable studies vary including the effects of the pitch-flap coupling, flapping hinge offset, natural frequencies of the blades/rotor, aerodynamic forces on the wing, and flight attitude [4]. Recently, research has been further conducted to extend the whirl-flutter stability boundaries by optimizing the blade twist [5].

The existing research regarding the whirl stability for the propeller and nacelle system has focused on either the stiffness or damping of the pylon/nacelle. In the effort, an engine-nacelle drive system was not entirely took into account [6]. In order to understand such influence, Rigo et al. attempted to analyze the effect by the load path upon the aeroelasticity by additionally considering the drive train [7]. Nonetheless, the scope in their study was too limited to consider the overall mechanical structure, by the modeling of the drive system as a lumped mass.

Recently, Future Long-Range Assault Aircraft (FLRAA) program by U.S. Army has led to the development of V-280 Valor aircraft by Bell Helicopter. From Army's request, there was a critical need to secure the safety from engine exhaust gas during the troop loads and unloads. For this reason, U.S. Army intended to maintain the use of the side doors for tactical purposes in an aircraft operation, which led to the design change where the engine remained fixed [8]. Only the rotor hub rotated from 0 to 90° as shown in Fig. 1.2.

Though, due to the limited information available for the drive system mechanism on the 'V280 Valor,' not any studies have been conducted yet regarding the effect of the change in engine-nacelle drive system mechanism. Nevertheless, it carries significant importance in that the mechanism implemented here, shows a totally different approach compared against the previous generation of the tiltrotor aircrafts.

Based on that background, a detailed design for an entire pylon system is attempted to observe the effect on the aircraft aeroelasticity. This thesis will show a difference by modeling the entire components in the drive system including the gear, shafts, bearing and the housing. Rigo et al. [7] attempted a similar approach but still employing the simple lumped mass for the drive-train system. A detailed modeling for the load path through the drive system will be important to evaluate the vibratory loads that are transmitted between the rotors and the engines [9]. Therefore, evaluating the aeroelastic effect by such an approach will hold a great implication.

In this thesis, engine-nacelle rotation mechanism of XV-15, as shown in Fig. 2(b), undergoes modifications by replacing it as shown in Fig. 2(a). Subsequently, an impact of the changes in the engine nacelle rotating mechanism will be investigated, based on the reference available for XV-15 [10].

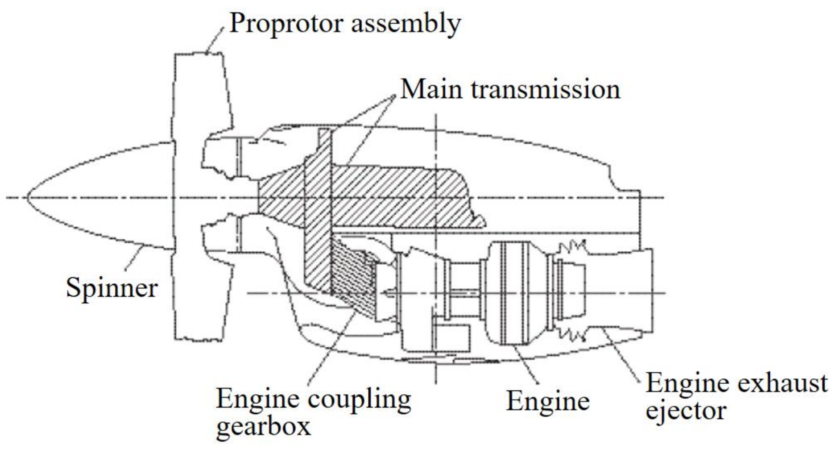

Fig. 1.1 'XV-15' nacelle arrangement [1]

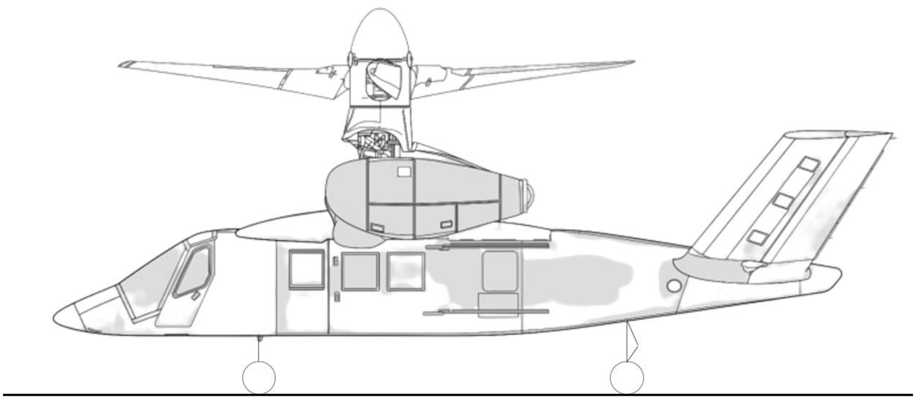

Fig. 1.2 ‘V280 Valor’ side view

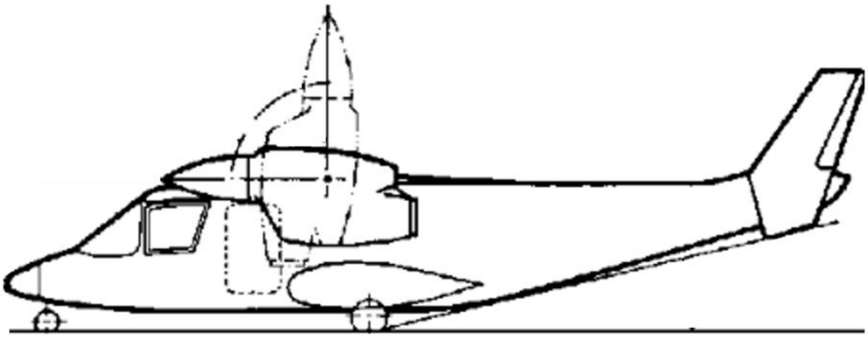

Fig. 1.3 XV-15 side view

1.2 Objectives and thesis overview

In this thesis, drive-system design for the engine-nacelle operating mechanism and the whirl flutter analysis is attempted. The aircraft for the present whirl flutter analysis is XV-15. The flow chart in Fig. 1.4 shows the sequence in which the research is performed. The entire procedure is characterized by the summaries as follows.

1. The engine-nacelle tilting mechanism is proposed based on 'V-280 Valor.' The components of the gearbox are designed in a top-down manner to incorporate the gear ratios and geometric configurations using ZAR/ROMAX, the gear design software and SOLIDWORKS.

2. The analysis object for whirl flutter is constructed, by modifying XV-15, and the conventional engine-nacelle tilting mechanism is changed. The aircraft is designed in one-dimensional stick representation, embodying the rigid body and flexible beam elements. And the present gearbox is implemented into the aircraft representation. The present drive system is incorporated into the analysis by using NASTRAN. Modal analysis is performed to examine the natural frequencies.

3. To investigate the influence of whirl flutter in the drive-system design, comparison is made between the newly implemented engine nacelle configuration and the original baseline found in the reference. The result is obtained by using CAMRAD II flutter analysis with the uniform flow aerodynamics.

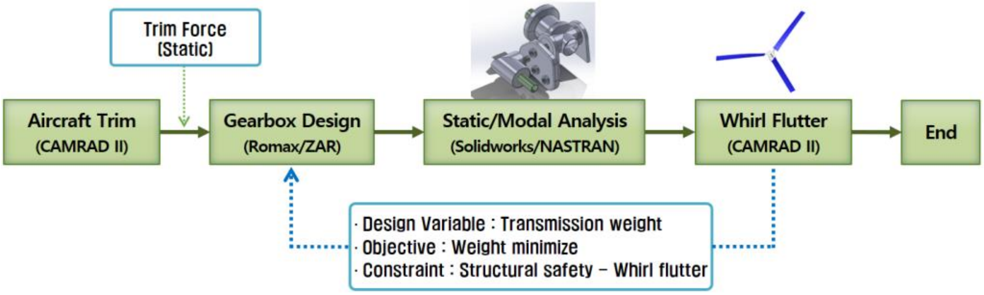

Fig. 1.4 Present analysis procedure

Chapter 2

Engine-Nacelle Drive System Design

In this chapter, the drive system for the engine-nacelle tilting mechanism will be designed. The reference drive system is created based on the hardware of V280 valor, developed for FLRAA. The load analysis for gear sizing condition will be performed including the free wake analysis in CAMRAD II. And the structural modeling is completed by the gear design software, ZAR/ROMAX and SOLIDWORKS, which is applicable for XV15 aircraft.

2.1 Baseline tiltrotor configuration

The baseline object for the analysis is selected as XV-15 tiltrotor aircraft. The estimated weight reports and geometries for the object are shown in Fig. 2.1 and Table 2.1. In this thesis, the approach of employing V280 engine nacelle drive system to XV-15 is executed. To take this into account, the entire drive system is designed considering the weight of the rotor hub and the actual engine. Only engine the cowling surrounding the engine is estimated by using AFDD82 weight estimation trend curve [11].

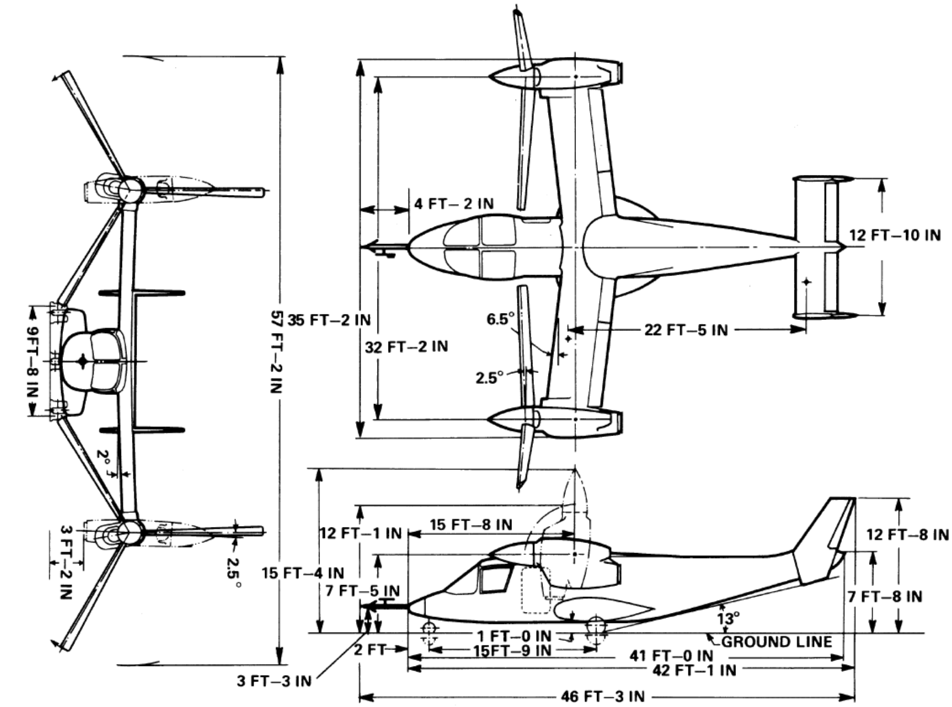

Fig. 2.1 XV-15 dimension three side view

Table 2.1 XV-15 aircraft weight breakdown

	NDARC XV-15 [12]	**Maisel XV-15 [1]**	**Magee XV-15 [13]**
Structure	**4664.6**	**4162**	**4230**
Propulsion	**2775.1**	**3017**	**2570**
└ Drive system	└1340.7	└1263	└1100
Flight control	**1112.3**	**934**	**1010**
Useful Load for DGW	**2899.3**	**3676**	**3924**
Fixed equipment	**1548.7**	**1211**	**1283 (2340)**
Gross Weight	**13000**	**13000**	**13000**

2.2 Gear theoretical background

2.2.1 Gear sizing method

The method for the gear design [14] is illustrated in Fig. 2.1. If two out of three parameters, power, rotational speed (RPM) and torque, are obtained, an initial sizing condition will be determined. And the application factor K_A will be applied for the worst-case operating condition. Considering an appropriate value of K_A, the design torque T_D is determines as

$$T_D = T_n \cdot K_A \tag{2.1}$$

where T_n is the nominal motor torque.

As the minimum module is obtained in the next step, the number of the gear teeth will be determined based on the gear ratio. After the material and the face width are chosen in the order, the gear strength will be estimated in the final step. Entire procedures are iterated until the condition for S_F and S_H, which represent the gear strength, are satisfied. ZAR is utilized for the present gear design, which provides an initial gear size based on ISO 6336 standard using trend-based equations.

In this thesis, the power and rotational speed (RPM) are obtained, and the initial gear ratio(u) is estimated in top-down manner to match the configuration of the gearbox. According to ISO 6336 standard, the gear width(C) is chosen as 10% of the module.

If the diameter of driving gear is initially sized for adequate contact fatigue strength, the minimum module required to avoid bending fatigue failure is obtained from

$$m_n = \frac{2\ T_D\ 10^3}{C\ d_1^2} \cdot \frac{S_F}{\sigma_{FP}} \cdot \mathrm{Y} \cdot K_{F\beta} \cdot K_v \qquad (2.2)$$

where the combined geometry and stress concentration factor Y approximates

For spur gears, Y=3.4,

For helical gears, Y=2.9.

K_v is the dynamic factor, to allow for inertial forces due to pitch profile error. $K_{H\beta}$, $K_{F\beta}$ are the face load distribution factors for contact and bending strength. The method of calculating K_v, $K_{H\beta}$, $K_{F\beta}$ used in this module is taken from DIN 3990 [14]. Meanwhile, the permissible stress in Eq. (2.3) and (2.4) are given by

$$\sigma_{FP} = \sigma_{FE} \cdot Y_N \cdot Y_X \sqrt{M_Q} \quad \text{(permissible bending stress)} \qquad (2.3)$$

$$\sigma_{HP} = \sigma_{Hlim} \cdot Z_N \sqrt{M_Q} \quad \text{(permissible surface stress)} \qquad (2.4)$$

where the factors modifying bending strength(σ_{FP}) are Y_N, the life factor for strength, Y_X, the size factor to account of the reduction in fatigue strength and M_Q, the material quality factor. And the factors modifying surface strength(σ_{HP}) are and σ_{Hlim}, the endurance limit and Z_N, the life factor. All those factors are selected from DIN 3990 in each iteration with appropriate manner.

As the minimum module is selected, the pinion diameter that satisfy the contact strength and bending strength are each determined from Eqs. (2.5) and (2.6).

$$d_1 = 700 \sqrt[3]{\left[\frac{S_H}{\sigma_{HP}}\right]^2 \cdot \frac{T_D}{C} \cdot \frac{u+1}{u} \cdot K_{H\beta} \cdot K_v} \qquad (2.5)$$

$$d_1^3 = \frac{2\ T_D\ 10^3}{C} \cdot \frac{Z_{1min}}{\cos\beta} \cdot \frac{S_F}{\sigma_{FP}} \cdot \mathrm{Y} \cdot K_{F\beta} \cdot K_v \qquad (2.6)$$

Figure 2.1 depicts the entire procedure for the present gear design.

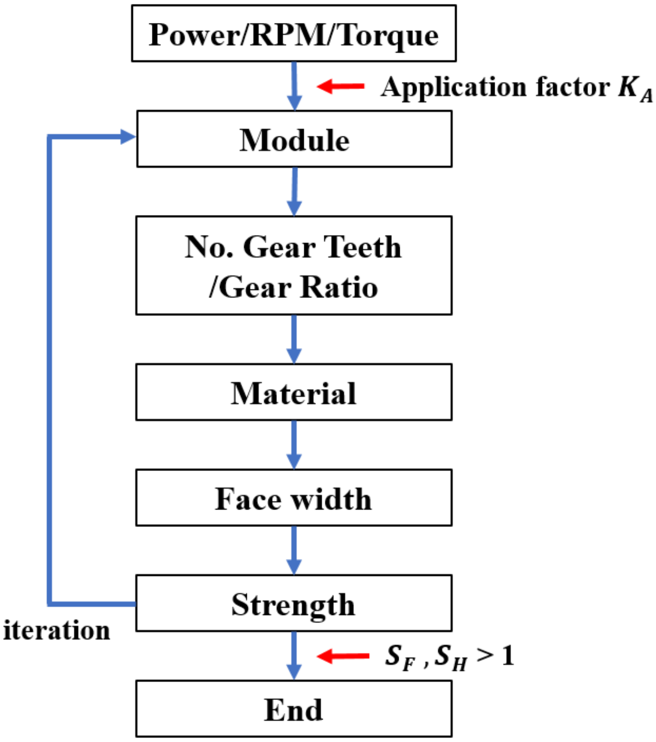

Fig. 2.2 Gear sizing flow chart

2.2.2 Gear ratio estimation

The drive system consists of the multiple stages of the gears. Reduction occurs at the meshing points between the driving gear and pinion gear. In the case of spur and bevel gears, reduction ratio(u) is proportional to the number of gear teeth or to the ratio of diameters as follows.

$$u = \frac{d_2}{d_1} = \frac{z_2}{z_1} \tag{2.7}$$

where d_1 and z_1 each denotes the pitch diameter and gear teeth of driving gear, and d_2 and z_2 for pinion gear.

For the higher reduction ratio in the drive system, the planetary gear is often adopted which is known as the epicyclic gears. It consists of three gears: a sun gear, a planet gear, and a ring gear. This configuration allows for the high gear ratios to be achieved within a compact volume compared to the spur gears. Unlike the simple spur gear set, the input and output gear must be selected among the three components, to achieve a desired reduction ratio. Many output options will be obtained by fixing one gear and providing input to another gear. However, this thesis will present a mechanism in which the ring gear is fixed and the carrier is driven by the sun gear to make a higher reduction ratio [15]. In terms of the number of gear teeth(z), the design conditions for the planetary gear system will be introduced as follows.

$$\begin{gathered} z_{carrier} = z_{sun} + z_{ring} \\ z_{carrier} = 3z_{sun} \\ z_{carrier} = z_{sun} + 2z_{planet} \\ z_{sun} + z_{ring} = \mathrm{N} \cdot k, \\ k = integer \end{gathered} \tag{2.8}$$

Equation (2.8) represents the number of the gear teeth condition for the carrier, the condition for the reduction ratio, the dimensional condition for planetary gear system to be determined and the condition for the number of pinion gears (N) in the system each.

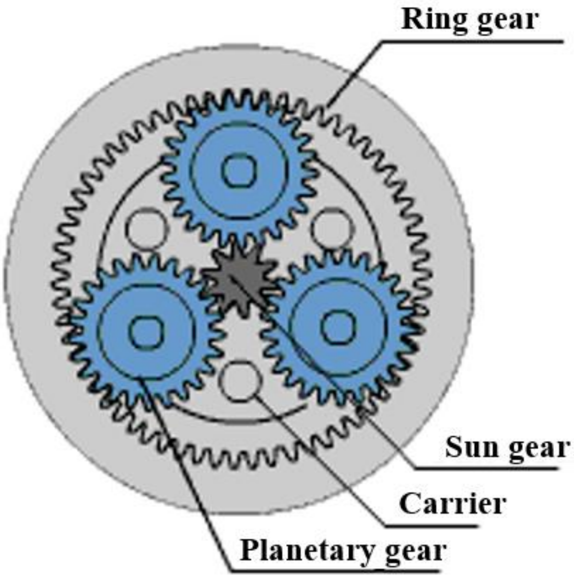

Fig. 2.3 Configuration of the planetary gear system

2.3 Drive-system mechanism

In this section, the mechanism for ‘V280 Valor’s hardware drive-system is introduced. The drive-system is divided into the following two components.

・ Power transmission system which transfers the power from the engine output to the rotor hub through the multiple gear stages.

・ Rotor-hub conversion system which rotates the rotor hub to enable the conversion between the helicopter and airplane mode

Figure 2.4 shows ‘V280 Valor’ tiltrotor aircraft and Fig 2.5 shows its internal structure of the engine-nacelle drive system for the left rotor hub [16]. The schematic representation of the mechanism is shown in Fig 2.5. The first stage is the bevel gear set driven by the engine, followed by the power transmitted to the gearbox. By incorporating an additional gearbox, the engine will maintain a horizontally while transmitting the power to another component. The power transmitted from the gearbox will then be transferred to the rotor mast via the second bevel gear set. And before the last stage, the rotor mast pass on the power to the rotor hub, a significant reduction is achieved through the two-stage planetary gear system.

As for the rotor-hub conversion system shown in Fig 2.6, a cylindrical gearbox is attached to the right side of the power transmission system, known as the rotor mast in Fig 2.3(b). By transmitting the power from the three of the power drive unit, this cylindrical gearbox enables the conversion of the aircraft between the fixed-wing mode and the helicopter mode. The internal configuration of the cylindrical gearbox is depicted in Fig 2.7, where the red boxes represent the gear reduction stages, and the blue box indicates the fixed condition. While the open literature [17] suggests a final gear ratio of 1100:1, there are uncertainties regarding the gear ratio in some sections. Taking this into account, the 2-stage differential planetary gear assembly is replaced by the 2-stage epicyclic gear system. The structure is depicted in Fig. 2.8, where the upper hydraulic power drive unit (HPDU 1) rotates the outer gear, which then goes through the 2-stage epicyclic gear system transmitting it to output shaft connected the rotor mast. In the case of a failure, HPDU 2 rotates the internal gear, following a similar pattern through the 2-stage epicyclic gear system to the output shaft.

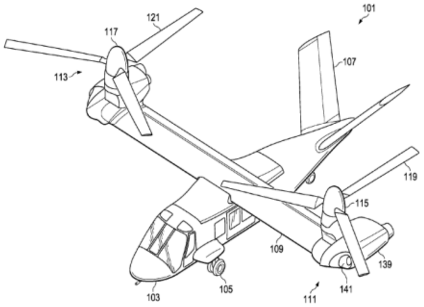

(a) Aircraft configuration

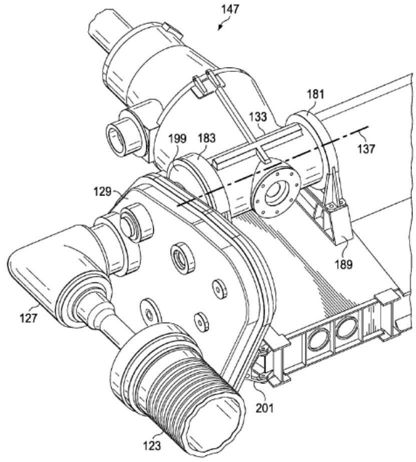

(b) Power transmission system

Fig. 2.4 Perspective view of ‘V280 Valor’

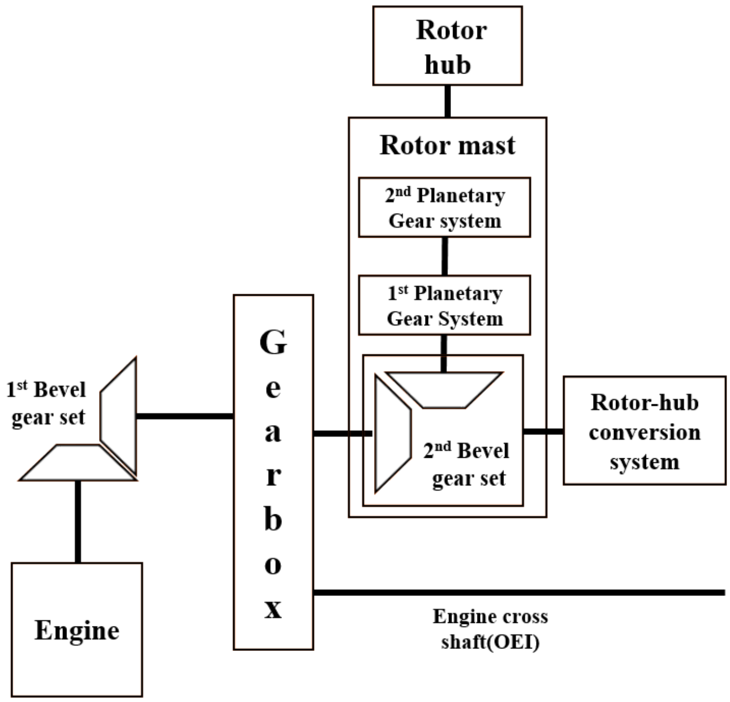

Fig. 2.5 Power transmission system diagram

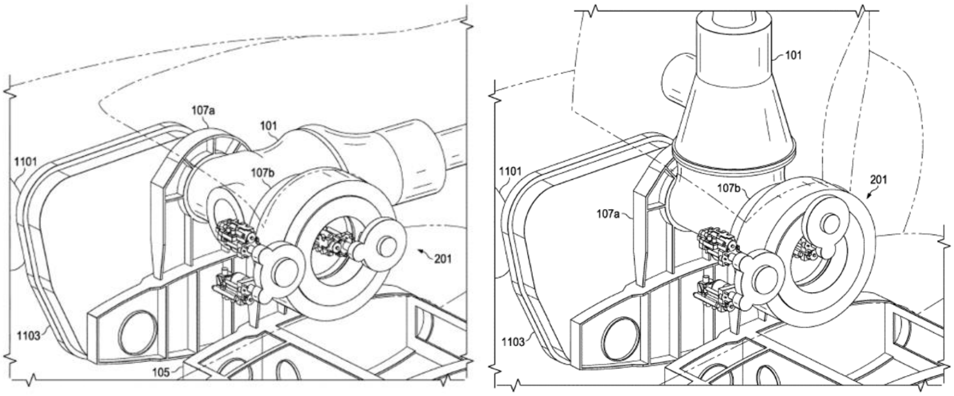

(a) Airplane mode (b) Helicopter mode

Fig. 2.6 Perspective view of tiltrotor in each mode

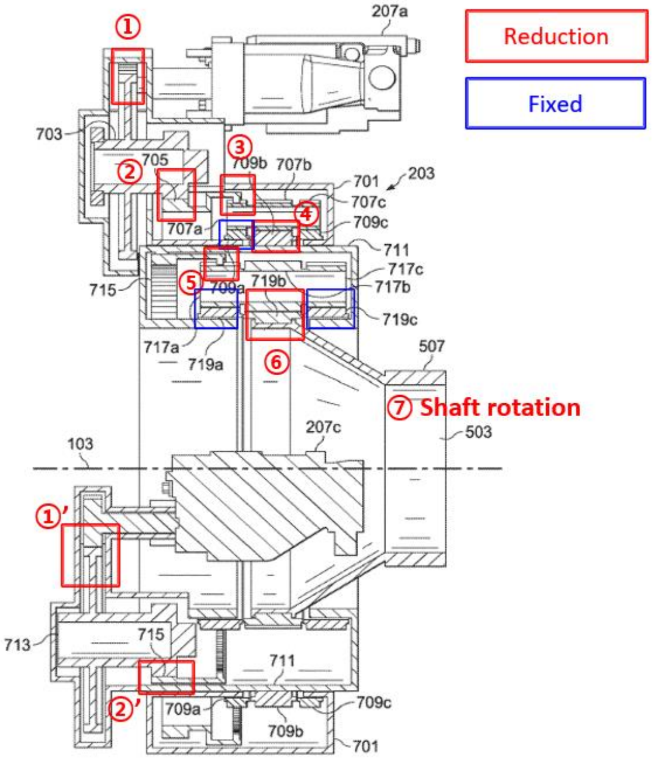

Fig. 2.7 Rotor-hub conversion system side view

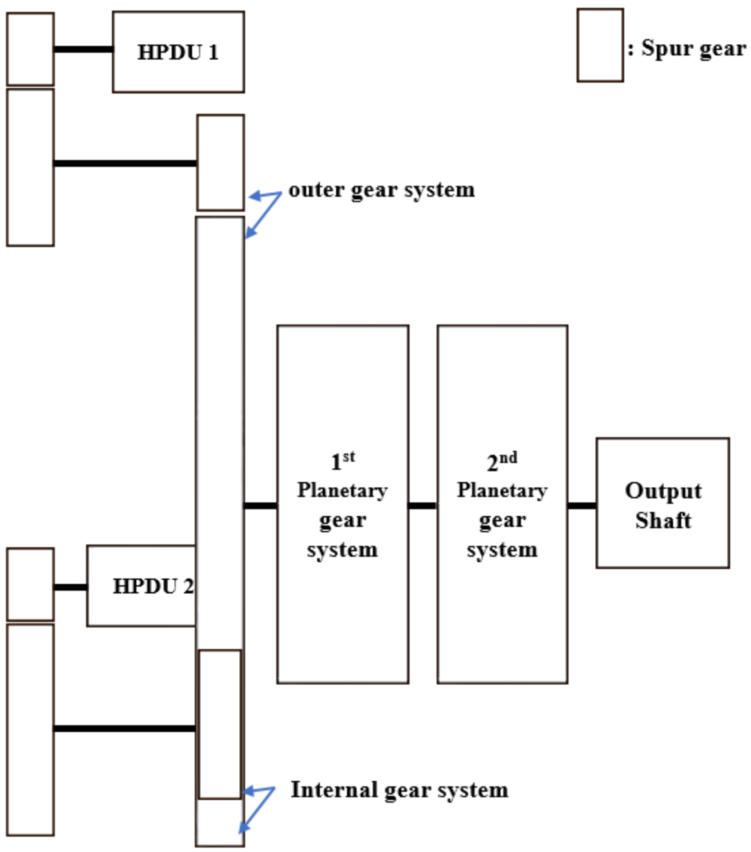

Fig. 2.8 Rotor-hub conversion system diagram

2.4 Gearbox load analysis

2.3.1 Power transmission system

The power transmission system delivers the power from engine to the rotor hub through the multiple gear stages. Therefore, the first bevel gear, directly connected to the engine needs to be designed with the utmost conservative condition. The load acting on the bevel gear stage was determined based on the operating condition of the actual engine, Lycoming T53-L-13 turboshaft engine as shown in Fig. 2.9.

Design torque is determined from the engine operating horsepower and revolution per minute (RPM). As the bevel gear is the very first structure where the power is transmitted from the engine, the highest level of application factor, 2.25 is applied for the worst-condition [18]. The total reduction ratio is determined to reduce the engine rotating speed from 19,486 RPM to rotor hover rotating speed of 589 RPM. The modules obtained from the first bevel gear are applied uniformly to the subsequent gear stages. The load condition, including the design input are shown in Table 2.2.

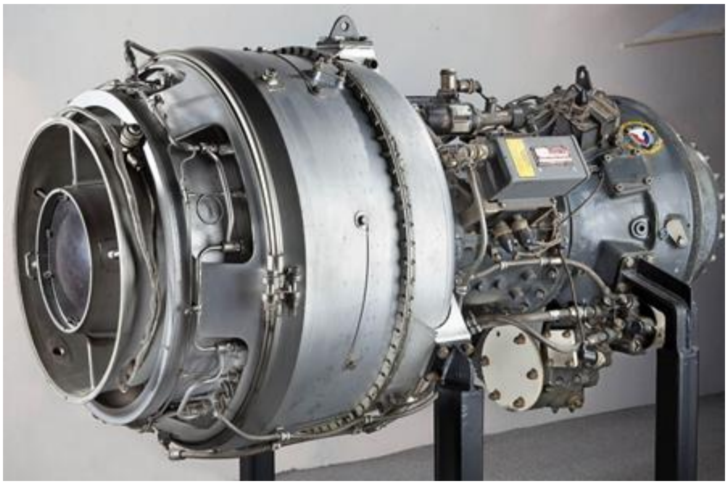

Fig. 2.9 Lycoming T53-L-13 (LTC1K-4) turboshaft engine

Table 2.2 Bevel sizing condition

Parameter	Value
Power (hp)	1,550
Rotating Speed (RPM)	19,486 RPM
Design Torque (ft·lb)	417.78
Application factor	2.25
Total Reduction Ratio	33 : 1

2.3.2 Rotor-hub conversion system

Rotor-hub conversion system enables the aircraft to achieve the ability for transition. As for considering the load condition, the rotor-hub conversion system will experience the large loads during the transition state. Therefore, in addition to the power supply from the hydraulic power drive unit, the forces due to the aerodynamic loads during transition should also be considered. Consequently, transition analysis is conducted to identify the point where the highest force is exerted on the gears.

The loads applied to the conversion axis can be reduced to a two-dimensional plane as shown in Fig. 2.10, where the dominant load is the pitching moment. The moment applied to the conversion axis C' is obtained by estimating the steady components of the thrust, horizontal force and pitching moment acting on the rotor hub.

F_x and F_y at point C can be obtained as Eq. (2.9)

$$\begin{aligned} F_x^C &= Hsin\theta - Tcos\theta \\ F_y^C &= Tsin\theta + Hcos\theta \end{aligned} \tag{2.9}$$

If the distance L between Point C and C' is determined, the pitching moment at C' will be defined as Eq. (2.10)

$$M_y^{C'} = M_y^C + F_x^C dsin\theta + F_y^C dcos\theta \tag{2.10}$$

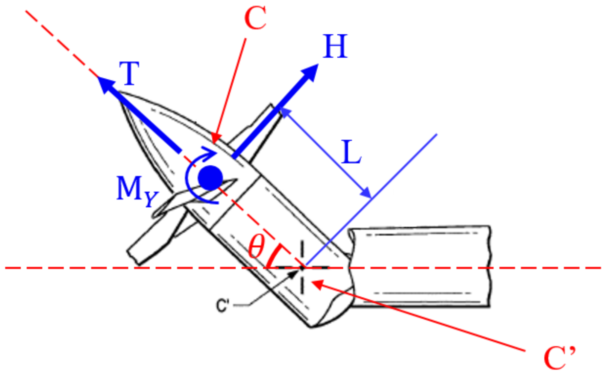

Fig. 2.10 Free body diagram of the conversion axis

Table 2.3 XV-15 Rotor properties

Parameter	Value
Number of blades	3
Rotor radius (ft)	12.5
Rotor solidity (σ)	0.089
Blade twist (°)	-40°
Hub precone (°)	2.5°

Table 2.4 Rotor aerodynamics input

Parameter	Value
Number of Trailers	2
Span stations	0.2, 1.0
Number of panels	15
Number of blade section	5
Gimbal	1

To obtain the hub load during its transition, CAMRAD II free wake model with quasi-steady analysis is performed for XV-15 isolated rotor blade. Table 2.3 shows the rotor blade property where analysis is conducted and the aerodynamic input condition are shown in Table 2.4.

To verify the input construction, a transition schedule for CFD and flight test data of XV-15 tiltrotor [19] are selected as reference shown in Table 2.5. Thrust is set as a trim target in 90, 75, 60, 30 and 0° at each point which shows an exact correspond in Fig 2.12(a). Thereafter, H-force and torque is compared against the flight test data and it is shown in Fig. 2.12(b) and (c).

Based on the result, the pitching moment applied to C' at each nacelle conversion angle is determined, as shown in Fig. 2.13. It can be seen that the load increases during the conversion as the nacelle angle gets smaller and the highest load is applied at 30°. The free wake models for each nacelle angle is presented in Fig 2.14.

As far as the pitching moment 2,886 ft · lb at 30° is determined, the rotating speed for conversion axis is assigned as1.25 RPM based on the transition schedule[2] of V-22 Osprey. The 2nd planetary gear system, at the end of the rotor-hub conversion axis was designed using static analysis since it is directly exposed to this highest pitching moment. The application factor is 1.5. The sizing condition for the 2nd planetary gear system is listed in Table 2.6.

Meanwhile, during the transition flight of a tiltrotor, the aerodynamic loads mainly experienced by the rotor blades are distributed to the wings. For this reason, wing stall must be taken into consideration with the conversion envelope as depicted in

Fig. 2.11 for XV-15. The six data points for the quasi-steady transition analysis are plotted in red dots. Among these, five are located in the safe regions away from the wing stall. However, at the 75° of nacelle angle, there is a lack of wing stall margin with relatively low speed of 40knots. Therefore, additional consideration is needed regarding this limitation. Nonetheless, since the highest load is not imposed at this point, the transition is performed following the existing reference [16].

Table 2.5 XV-15 Transition schedule [16]

Configuration	Wind (knots)	RPM	Nacelle Angle(°)	Tip speed(ft/s)
Hover	0	589	90	771
Conversion Mode	40	589	75	771
Conversion Mode	100	589	60	771
Conversion Mode	140	589	30	770
Cruise	160	517	0	669
Cruise	200	517	0	669

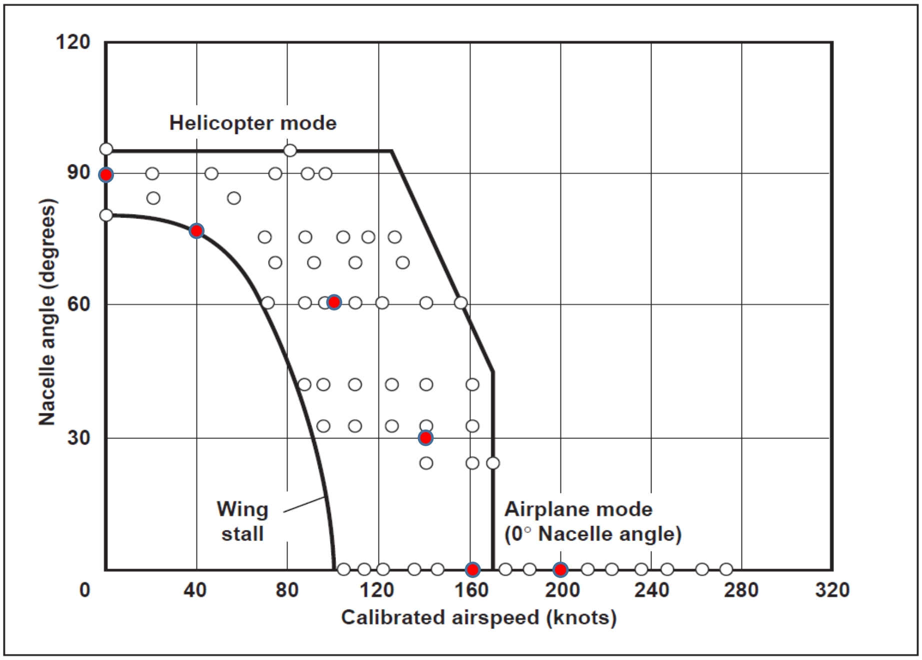

Fig. 2.11 Conversion corridor of the XV-15 tilt rotor research aircraft [1]

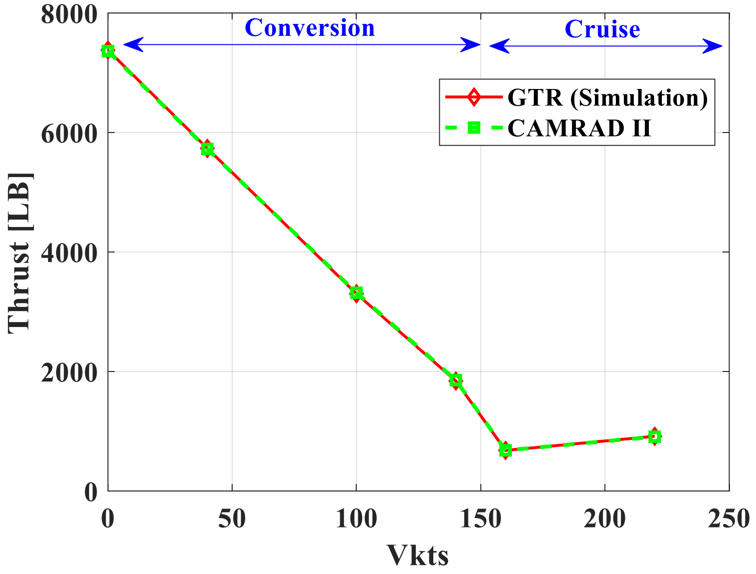

(a) Thrust trim target

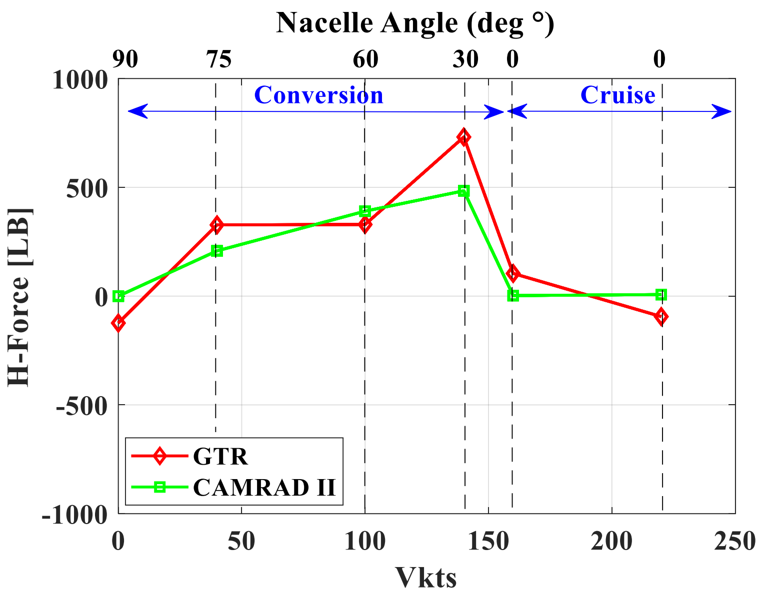

(b) H-force comparison

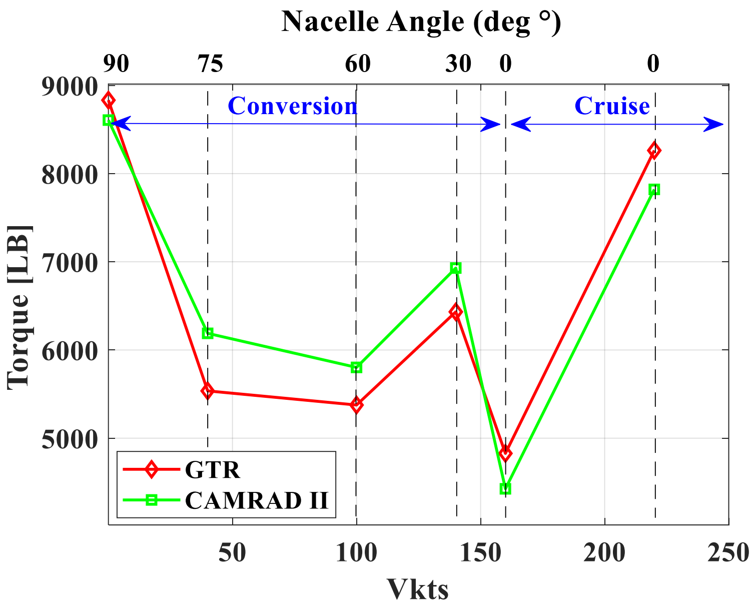

(c) Torque comparison

Fig. 2.12 Rotor-hub load comparison during the transition

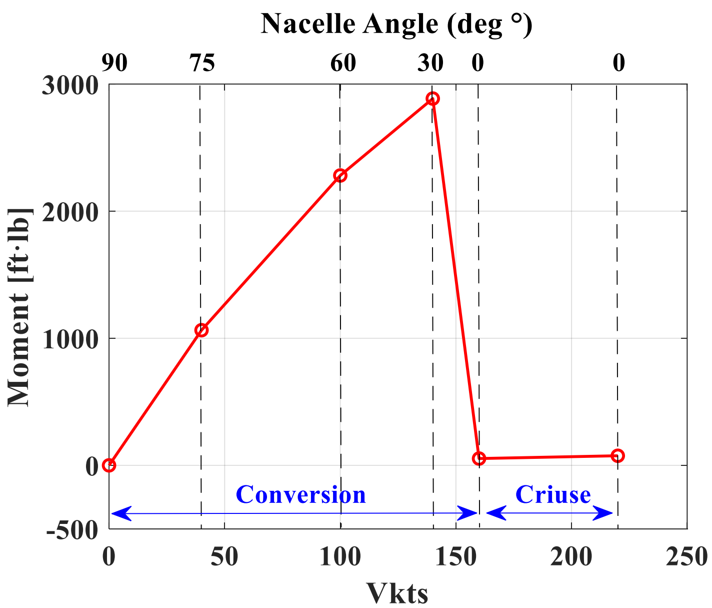

Fig. 2.13 Pitching moment at the conversion axis

Table 2.6 Planetary gear sizing condition

Parameter	Value
Pitching moment (ft・lb)	2,886
Rotating speed (RPM)	1.25
Application factor	1.5
Total reduction ratio	1100 : 1

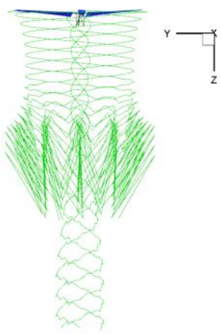

(a) Nacelle angle 90°

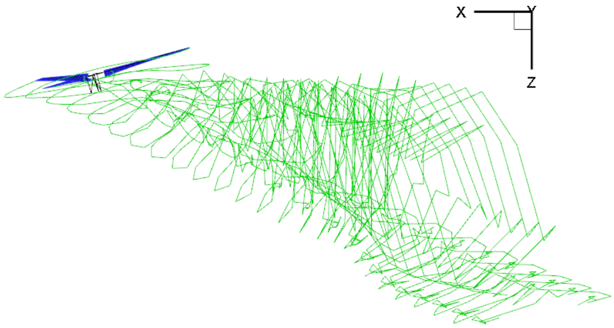

(b) Nacelle angle 75°

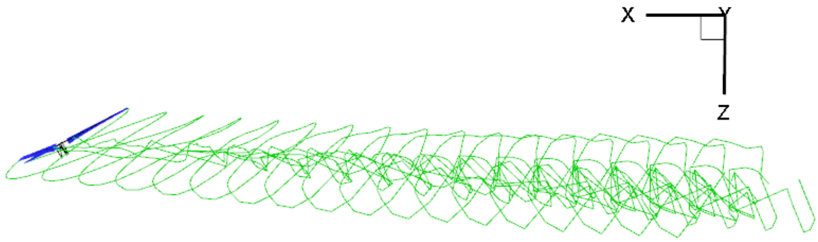

(c) Nacelle angle 60°

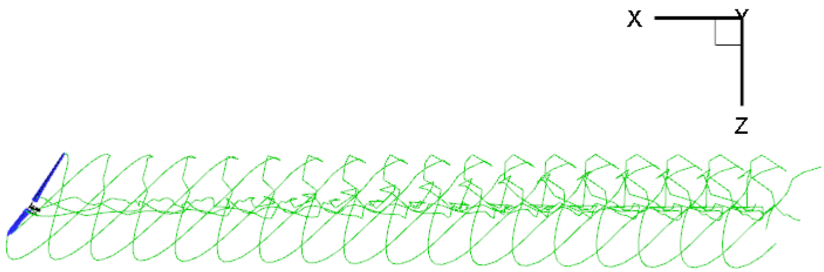

(d) Nacelle angle 30°

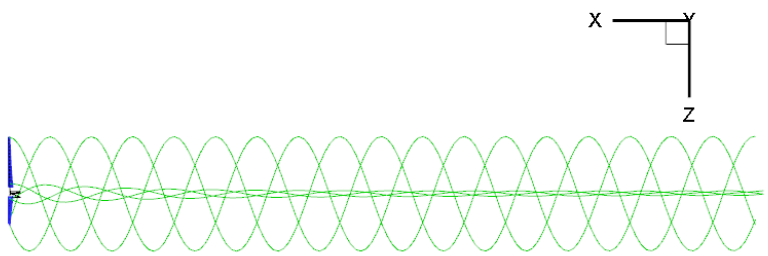

(e) Nacelle angle 0°

Fig. 2.14 Rotor free wake at each nacelle angle

2.5 Analysis results

In this section, the design results derived from the load analysis are presented. For the power transmission system, the required load for the initial bevel gear stage, which is connected to the engine was determined. Based on the results, the bevel gears are sized, and the subsequent gear stage are designed in a top-down manner to achieve the total reduction ratio and geometric similarity with XV-15 aircraft. The safety factor for the bevel gear design is shown in Table 2.7, and the reduction ratios and gear geometry for each stage are presented in Table 2.8. Figure 2.15 illustrates the design results of the gears.

For the rotor-hub conversion system, the pitching moments on the conversion axis at each nacelle angle are estimated. Based on the results, the 2nd epicyclic gear system, where the highest loads are applied, is designed. Then, subsequent gear stages are designed to achieve the total reduction ratio. The design results are presented in Tables 2.9 and 2.10. Figure 2.16 depicts the completed gear design before enclosing it into the housing.

Thereafter, the housing enclosing the gears is constructed. The design is aimed at achieving the lower weight by considering the gear rotational radius and the outer radius of the bearings. The completed configuration for the drive system with the housing covered is shown in Fig 2.17. The weights of each group components are presented in Table 2.11. And the materials are applied according to the most common for gearbox design [20, 21].

Table 2.7 Safety factor for the first bevel gear set

	Driving gear	Pinion gear
S_F	1.44	1.21
S_H	1.27	1.06

Table 2.8 Power transmission system design result

	Type	Reduction Ratio (u)	Module (m)	Pitch circle diameter (mm)	Material
1	Spiral Bevel Gear	1.3 : 1	5	Input: 244.5 Output: 189.2	AISI 4340 (17CrNiMo6)
2	Gearbox	1.4 : 1	5	Input: 170.0 Output: 235.0	
3	Spiral Bevel Gear	2 : 1	5	Input: 183.1 Output: 366.2	
4	1st planetary gear system	3 : 1 (Carrier/Sun)	5	Ring gear: 360	
5	2nd planetary gear system	3 : 1 (Carrier/Sun)	5	Ring gear: 540	
		32.7 : 1			

(a) Modeled profile

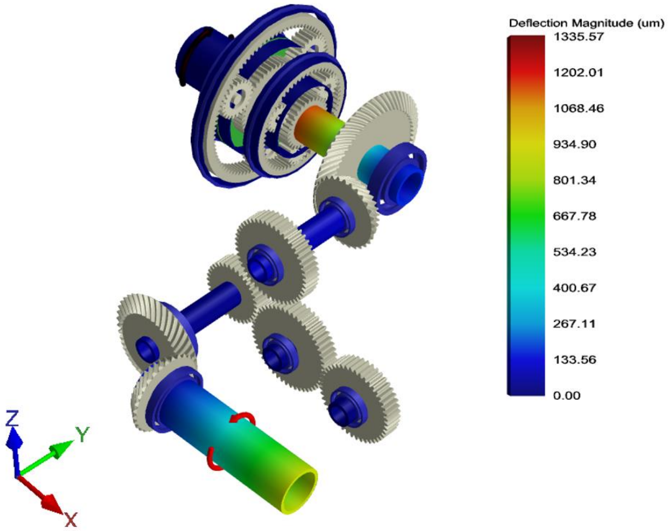

(b) Deflection magnitude

Fig. 2.15 Power transmission system configuration

Table 2.9 Planetary gear sizing safety factor

	Sun Gear	Carrier Gear	Ring Gear
S_H (Sun and Carrier)	1.02	1.07	
S_H (Carrier and Ring)		2.46	2.56
S_F (Sun and Carrier)	3.85	2.55	
S_F (Carrier and Ring)		2.80	4.35

Table 2.10 Rotor-hub conversion system design result

	Type	Reduction Ratio (u)	Module (m)	Pitch circle diameter (mm)	Material
1	HPDU : Gear1	4.82 : 1	3	Input: 51.0 Output: 246.0	AISI 4340 (17CrNiMo6)
2	Gear2 : Gear3	6.23 : 1	3	Input: 120.0 Output: 747.0	
3	1st planetary gear system	6 : 1 (Carrier/Sun)	3	Ring gear: 300	
4	2nd planetary gear system	6 : 1 (Carrier/Sun)	3	Ring gear: 300	
*	Redundancy Gear	25 : 1 (Carrier/Sun)	3		
		1100 : 1			

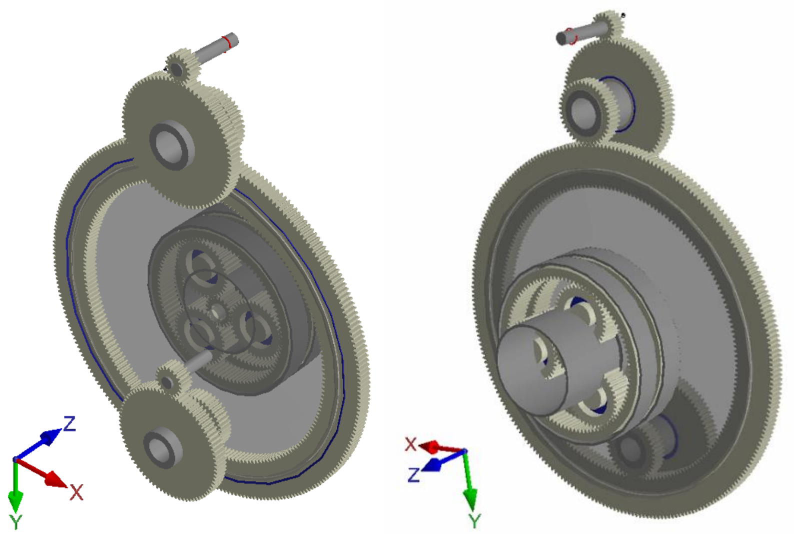

(a) Modeled profile

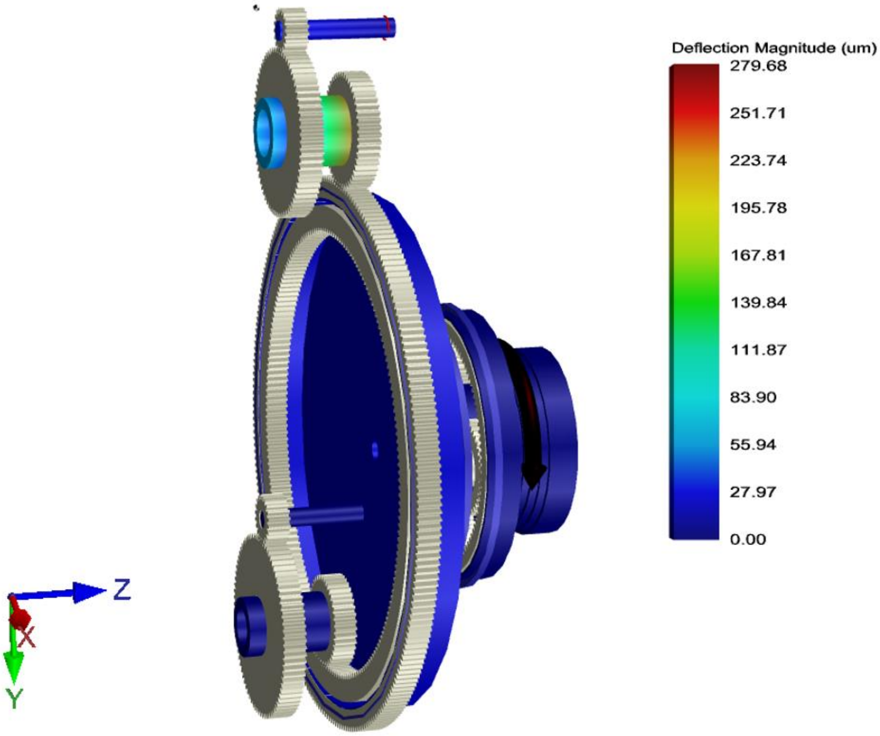

(b) Deflection magnitude

Fig. 2.16 Rotor-hub conversion axis configuration

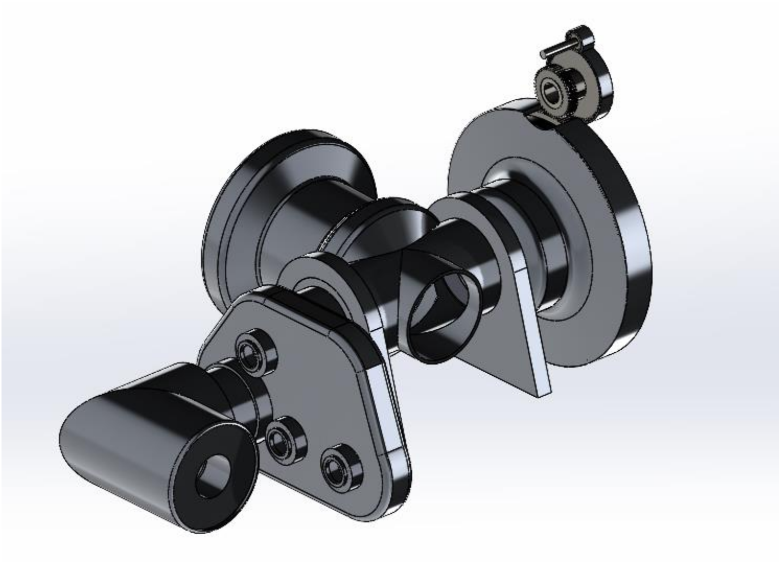

Fig. 2.17 Drive system mounted configuration

Table 2.11 Drive system weight

Component	**Weight (lb)**
Power transmission system	498.2
Rotor-hub tilting system	238.1
Housing	456.4
Single side	1192.7
Total drive system weight	**2385.4**

Table 2.12 Drive system component material property

	Material	E(GPa)	Poisson ratio (ν)	Density (kg/m^3)
Shaft	Cast alloy steel	190	0.26	7300
Bearing	Cast alloy steel	190	0.26	7300
Gear	AISI 4340	205	0.285	7800
Housing	1060 Aluminium Alloy	69	0.33	2700

Chapter 3

Structural Analysis

In this chapter, an analysis object of XV-15 structure is constructed to investigate the effect of the present drive system, as discussed in Chapter 2. The analysis model is validated by the mode analysis with NASTRAN, and the drive system is incorporated into the representation. Finally, the results of the wing modal outputs to conduct the whirl flutter analysis will be obtained.

3.1 Aircraft model construction

3.1.1 Baseline aircraft configuration

Based on the literature [10], the structural model of the airframe can be obtained as a simplified stick representation as shown in Fig. 3.1. It consists of elastic wing with beam elements, rigid fuselage and rigid wing-mounted nacelles. The primary objective of the initial XV-15 stick representation is to accurately demonstrate the six lowest natural frequency modes of the wing. For the validation, modal analysis for XV-15 airframe structure with a 23% thick wing is performed and it shows consistency with the wing six lowest natural frequency modes from the baseline stick representation used in the reference. Analytic results from this arrangement had shown good agreement with the detailed finite-element input construction [22] shown in Fig. 2.17, therefore, adopting the simplified input for the analysis is a feasible approach.

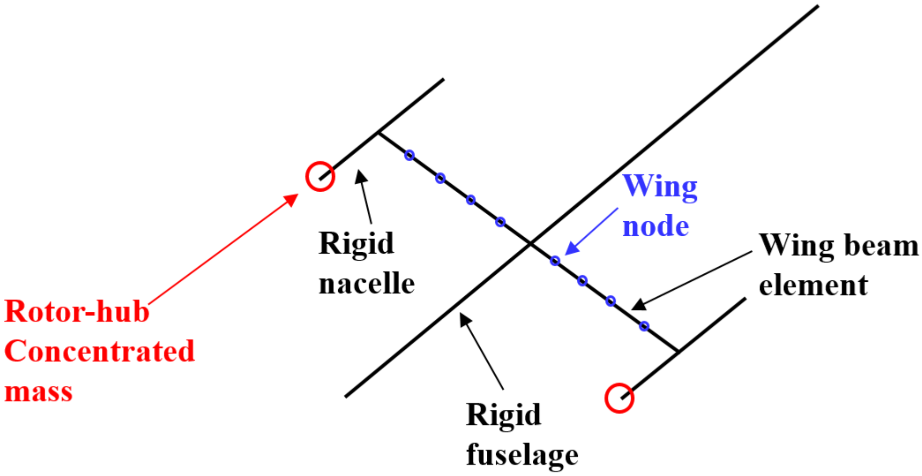

Fig. 3.1 XV-15 finite-element stick representation

Table 3.1 XV-15 finite-element stick-representation characteristics

Component	Element type	Number of elements	Length, ft	Weight, lb
Wing	Elastic beam	10	32.4	2,534
Left and right nacelle	Rigid beam	4	7.7	3,166
Left and right rotor	Concentrated mass	2	0	1,118
Fuselage	Rigid beam	2	42.1	6,182
			Gross weight	13,000

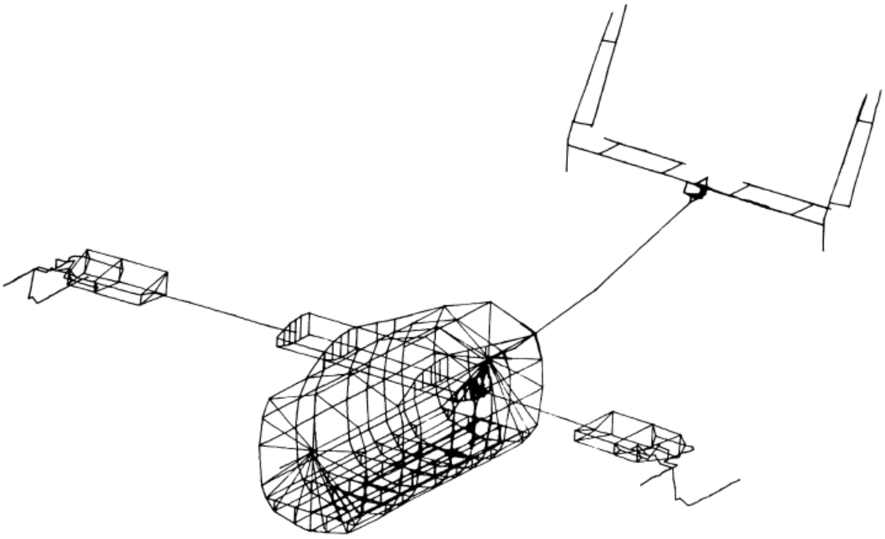

Fig. 3.2 XV-15 detailed finite-element input construction [20]

3.1.2 Modified aircraft representation

Including the mass of the actual engine and rotor hub, an overall structure of the engine-nacelle drive system is modified from the baseline configuration as shown in Fig. 3.3. The elasticity of the drive system is considered, as each of the components in the gearbox is applied with the proper material properties. Due to the increased weight of the engine-nacelle drive system, the gross weight of the aircraft has increased by approximately 5%. Total of 292,338 elements are generated in the preprocessing and the characteristics of the modified aircraft representation are presented in Table 3.2.

Figure 3.4 shows the configuration with drive systems attached to both wings. The drive system is mounted at the wingtip, and the ends of the mounting and the gearbox are bonded with RB2 elements, as shown in Fig. 3.5, where the mesh is generated. For the rotor hub and engine, only the mass is considered with the concentrated mass. Figure 3.6 shows the location where the concentrated mass is applied. The rotor hub is offset from the x-y plane to the position of the rotor mast axis. The engine and engine cowling mass are applied together, where the concentrated mass is applied on the CG point of engine. Since the weight of the engine cowling is relatively low, estimated weight data from available references [11,12] are adopted. The weight of the engine cowling is approximated as follows.

$$W_{cowl} = \chi_{cowl} \; 0.2315 \; S_{nac}^{1.3476} \qquad (3.1)$$

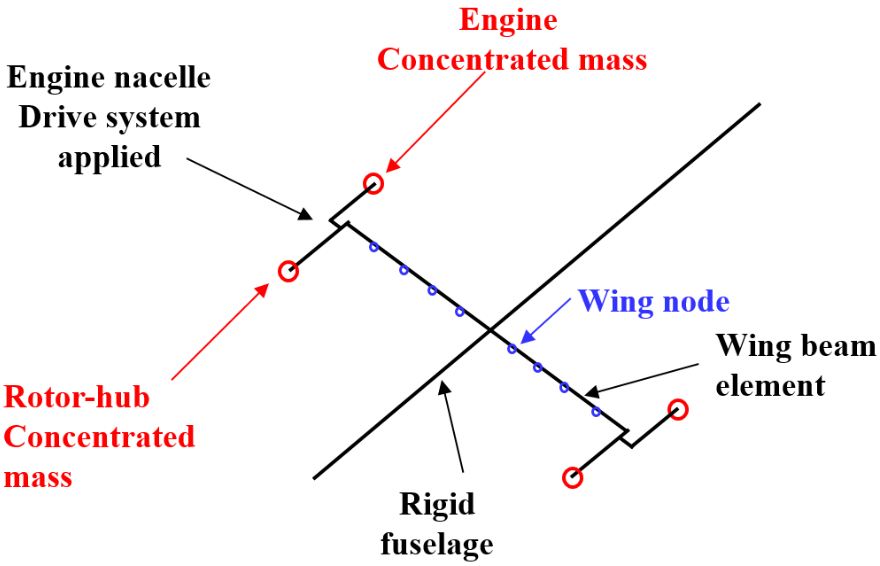

Fig. 3.3 Modified XV-15 finite-element stick representation

Table 3.2 XV-15 finite-element stick-representation characteristics

Component	Element type	Number of elements	Length, ft	Weight, lb
Wing	Elastic beam	10	32.4	2,534
Left and right rotor	Concentrated mass	2	0	1,118
Fuselage	Rigid beam	2	42.1	6,182
Engine and cowling	Concentrated mass	2	0	720
Drive-system	**Flexible body**	**292,338**		**2,496**
			Gross weight	13,770

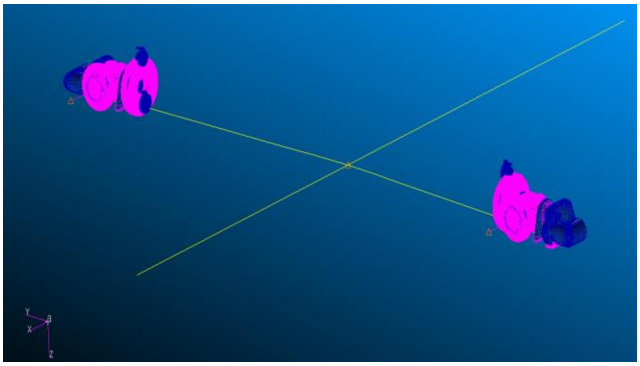

Fig. 3.4 Modified XV-15 finite-element stick representation (NASTRAN)

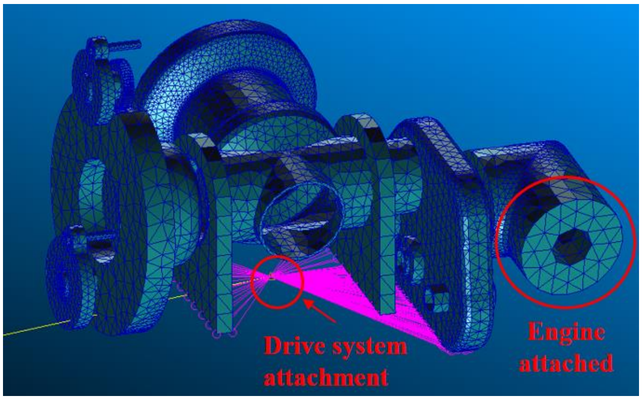

Fig. 3.5 Drive system attachment on main wing

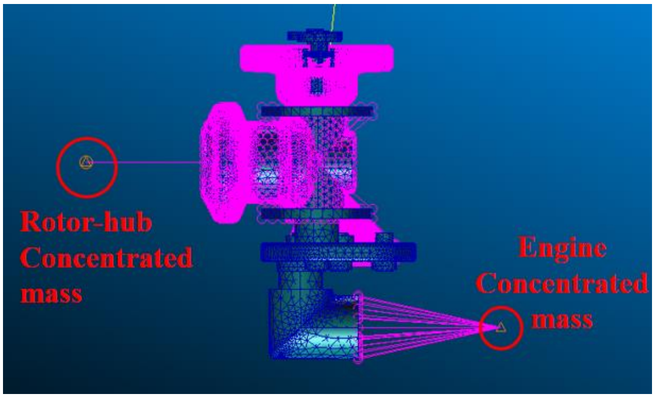

Fig. 3.6 Concentrated mass profile

3.2 Numerical results

After the analytic model construction, the modal analysis is performed by NASTRAN. The mode labels presented in Fig. 3.7 are somewhat arbitrary because the mode shapes rarely show pure bending, torsion, or chord-wise deflections. However, they exhibit an exact consistency in the mode shape with the 1st modes of the six lowest natural frequencies from Reference [10]. And it indicates that the baseline object to perform the flutter analysis is validated in an appropriate manner. Building upon this representation, the modifications are made to the baseline configuration in Section 3.1.1.

In the modified aircraft representation, the six lower-frequency modes exhibited the similarity with the baseline object, as shown in Fig. 3.8. The 1st symmetric mode shows resemblance in that each of the wing bending, wing chord and torsion mode occurred in the same order with the baseline representation. In the 1st anti-symmetric mode, the order in the appearance between the wing chord mode and the torsion is reversed. It is found that the change in the drive-system which generated the cross-section in the torsional axis, brought about the increase in the torsional stiffness. However, the inertia of the engine, which remains horizontally at the wingtip, may have a major effect on delaying the torsional mode.

Meanwhile in both 1st symmetric and 1st anti-symmetric modes, the increased weight of the engine nacelle drive system resulted in a general decrease in mode frequencies. The translational and rotational eigenvectors for each mode are obtained to perform the flutter analysis, and Table 3.3 represents the results.

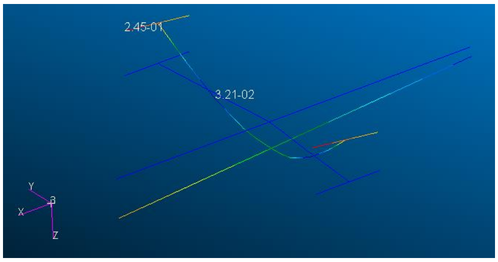

Symmetric bending mode (3.3Hz)

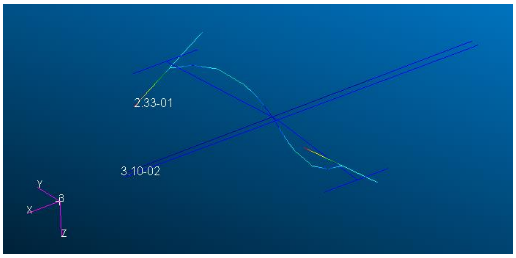

Anti-symmetric bending mode (6.3Hz)

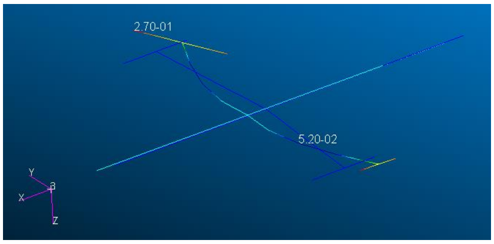

Symmetric chord mode (6.3Hz)

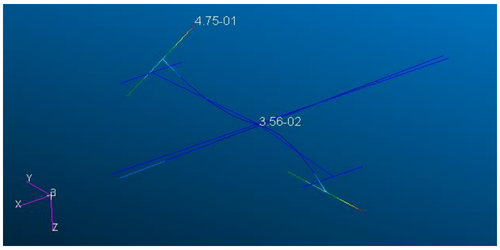

Anti-symmetric chord (8.7Hz)

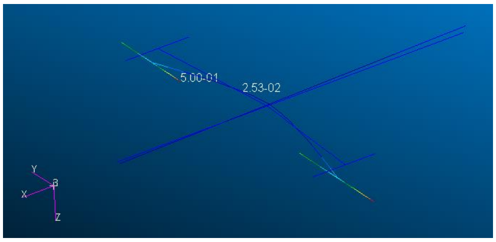

Symmetric torsion mode (8.3Hz)

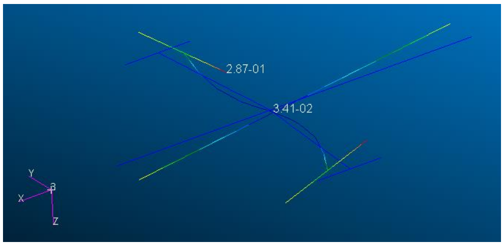

Anti-symmetric torsion mode (7.1Hz)

Fig. 3.7 Modified XV-15 stick-representation mode shapes and frequencies (0.23-t/c wing)

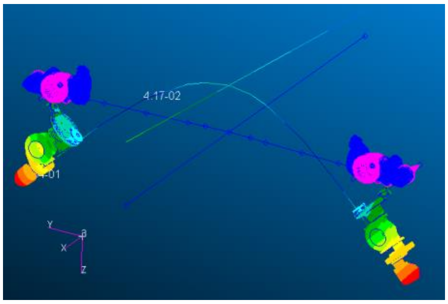

Symmetric bending mode (3.0Hz)

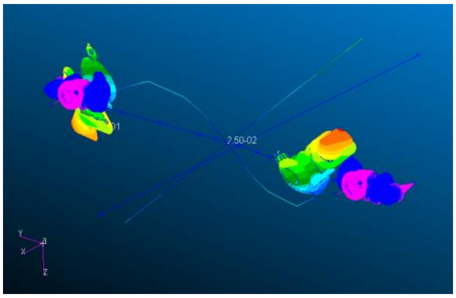

Anti-symmetric bending mode (6.1Hz)

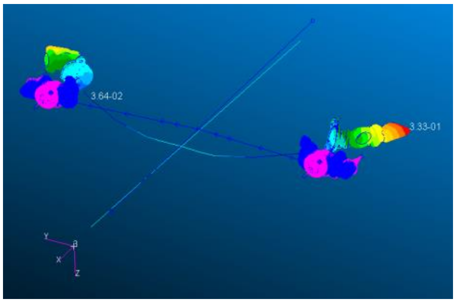

Symmetric chord mode (5.7Hz)

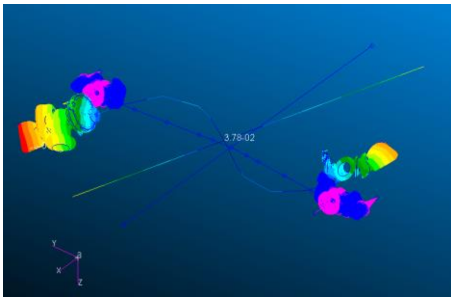

Anti-symmetric chord (6.6Hz)

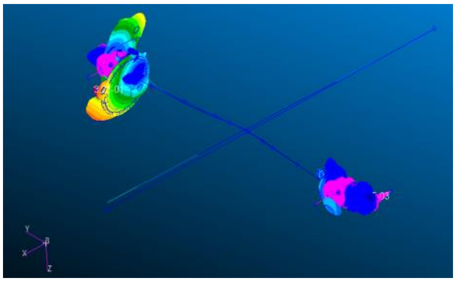

Symmetric torsion mode (7.9Hz)

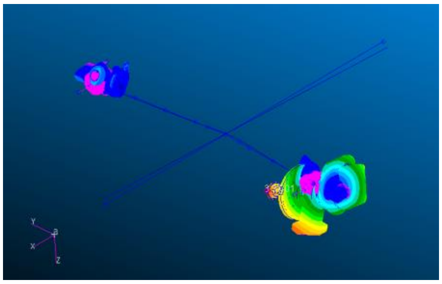

Anti-symmetric torsion mode (7.7Hz)

Fig. 3.8 Modified XV-15 stick-representation mode shapes and frequencies

(0.23-t/c wing)

Table 3.3 Mode shapes at the right hub for XV-15 finite-element stick representation

Mode	Symmetric beam	Symmetric chord	Symmetric torsion	Anti-symmetric beam	Anti-symmetric chord	Anti-symmetric torsion
Frequency, Hz	3.0	5.7	7.9	6.1	6.6	7.7
Displacement, ft						
X	$1.8\cdot 10^{-3}$	$-1.7\cdot 10^{-1}$	$-1.0\cdot 10^{-1}$	$1.5\cdot 10^{-1}$	$-5.9\cdot 10^{-2}$	$1.9\cdot 10^{-2}$
Y	$4.6\cdot 10^{-2}$	$1.5\cdot 10^{-1}$	$1.2\cdot 10^{-1}$	$-5.3\cdot 10^{-2}$	$-7.4\cdot 10^{-2}$	$8.7\cdot 10^{-2}$
Z	$1.8\cdot 10^{-1}$	$-7.7\cdot 10^{-2}$	$-2.6\cdot 10^{-3}$	$1.6\cdot 10^{-1}$	$-5.4\cdot 10^{-1}$	$5.4\cdot 10^{-1}$
Rotation, rad						
X	$2.7\cdot 10^{-3}$	$1.7\cdot 10^{-4}$	$2.2\cdot 10^{-3}$	$1.2\cdot 10^{-3}$	$9.7\cdot 10^{-4}$	$-1.3\cdot 10^{-3}$
Y	$9.2\cdot 10^{-5}$	$1.5\cdot 10^{-3}$	$1.3\cdot 10^{-3}$	$-2.4\cdot 10^{-3}$	$1.0\cdot 10^{-2}$	$-1.1\cdot 10^{-2}$
Z	$9.0\cdot 10^{-6}$	$2.5\cdot 10^{-3}$	$1.2\cdot 10^{-3}$	$-1.9\cdot 10^{-3}$	$-1.3\cdot 10^{-3}$	$1.9\cdot 10^{-3}$

Chapter 4

Tiltrotor Whirl Flutter Analysis

In this chapter, the whirl flutter analysis is conducted based on the modified representation using CAMRAD II. Two different trim condition is applied, and the critical damping is compared between the baseline and the modified representation to set the whirl mode boundary.

4.1 Trim condition

Whirl flutter occurs due to in-plane mode excitation and it makes the power of the rotor to decrease, converging to the zero. In the worst case, generating the power instead, the rotor absorbs the power from the wind, which leads to an aeroelastic unstable status in the lead-lag direction. Considering the phenomenon, two cases are analyzed to determine the whirl mode boundary.

In the first case, the constant rotor power condition is considered, where the trim target of the power is set as -1000hp. In the second case, the worst case is assumed that the rotor absorbing the wind power which is followed by the whirl flutter occurrence. This is achieved by setting the rotor trim power to the amount of worst case at each velocity. The rotor trim power boundary is set as -2000 to -7000hp and the corresponding worst trim power is applied at each cruise speed. The governor and the longitudinal cyclic are set as trim variables to adjust the drive train's torque and the vertical force F_z.

The rotor is trimmed to 458 rpm (76% of hover design rpm) at sea-level standard conditions. The analysis is performed in the speed range between 150 to 400knots true airspeed, with trim and stability obtained at 25-knot increment. In the second case, the trimmed result is obtained in every 10-knots between 300 to 400knots to take a closer look in detailed outcomes.

Uniform inflow with 15 aerodynamic panels and 2 structural nodes are applied as well as the open literature [10]. The structural damping is set to be 6% and the wing mode information for eigenvectors, mode frequencies and moment of inertia are used as input. The pitch-flap angle is set as -15°.

4.2 Analysis result

The results for the two conditions are shown in the figure. The dashed lines represent the result of the baseline object, while the solid lines indicate the modified aircraft representation outcomes.

In the first case, the rotor power is trimmed to -1000hp, a constant power at each velocity. In the 1st symmetric mode, the wing beam, wing chord and torsion mode occurs in the same order as the baseline case. The tendency of the frequencies is lower than reported in the literature. In the 1st anti-symmetric mode, a reversal is observed in the occurrence of order for the wing chord mode and torsion mode. And it is indicated by the red solid line (torsion mode) following the wing chord mode of the baseline object represented by the blue dashed line. Similarly, the blue solid line (chord mode) follows the torsion mode of the baseline object represented by the red dashed line. This demonstrates that the modified model's whirl mode does not deviate significantly from the reference literature [10]. Both the symmetric and the anti-symmetric modes exhibit the positive value for critical damping in the entire examination region.

The second case represents the worst case scenario. The overall frequency trends are not significantly different from Case 1, but there are notable differences in critical damping. In the symmetric mode, the critical damping value drops to -2.2% at 300knots in the torsion mode. And it differs from the baseline object in that the instability show in the chord mode at 350knots. In the anti-symmetric mode, the critical damping shows a steeper drop in value of -3.7% at 300knots for the modified input. This is attributed to the drive system characteristics, where the engine remains horizontally aligned. The structure supporting the engine horizontal alignment may experience high loads at high speed due to the vibration of the engine. Therefore, it is recommended to consider additional structures, such as the engine horizontal alignment device or to increase the torsional stiffness of the engine mounting component.

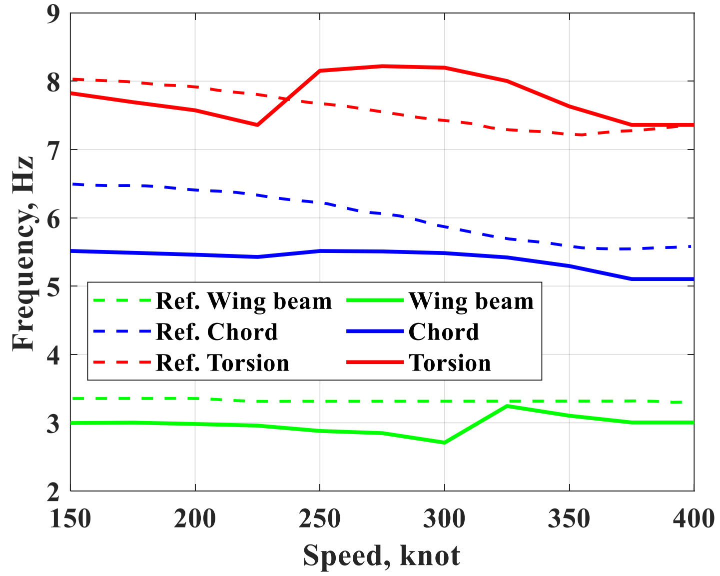

(a) Whirl-mode frequency versus airspeed

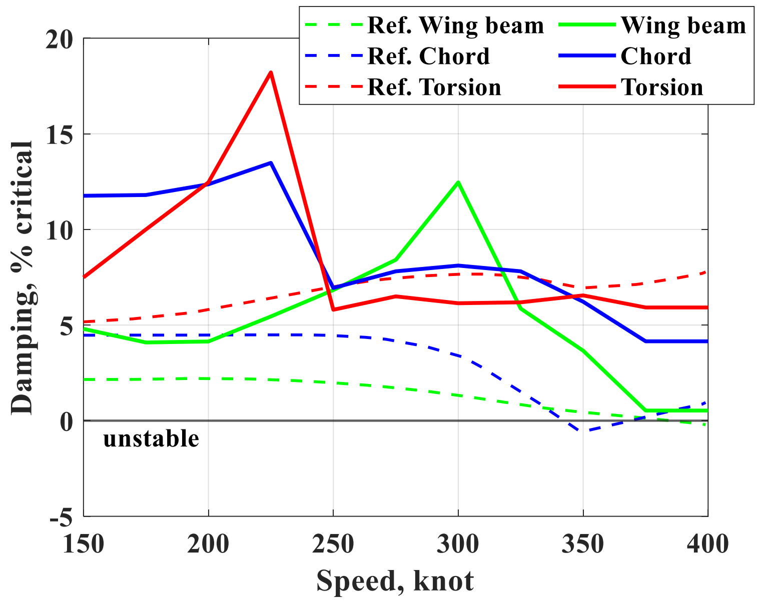

(b) Whirl-mode damping versus airspeed

Fig. 4.1 Symmetric whirl mode for Case 1

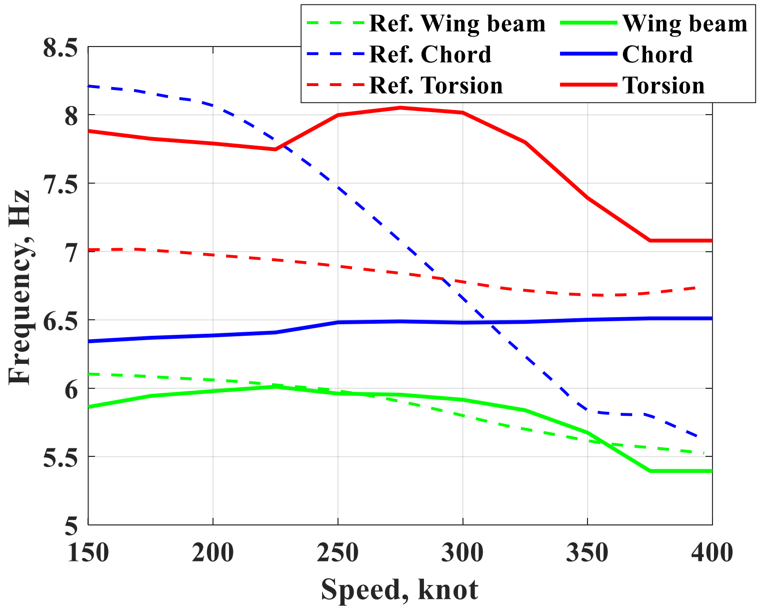

(a) Whirl-mode frequency versus airspeed

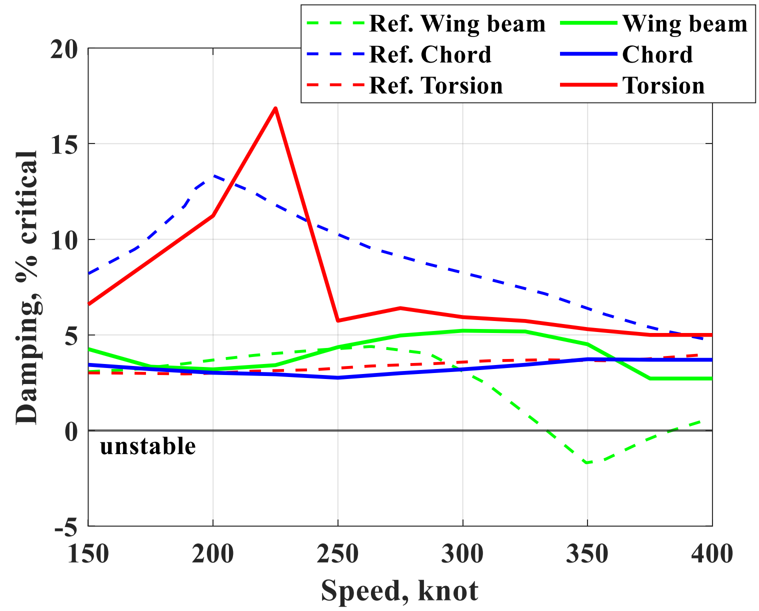

(b) Whirl-mode damping versus airspeed

Fig. 4.2 Anti-symmetric whirl mode for Case 1

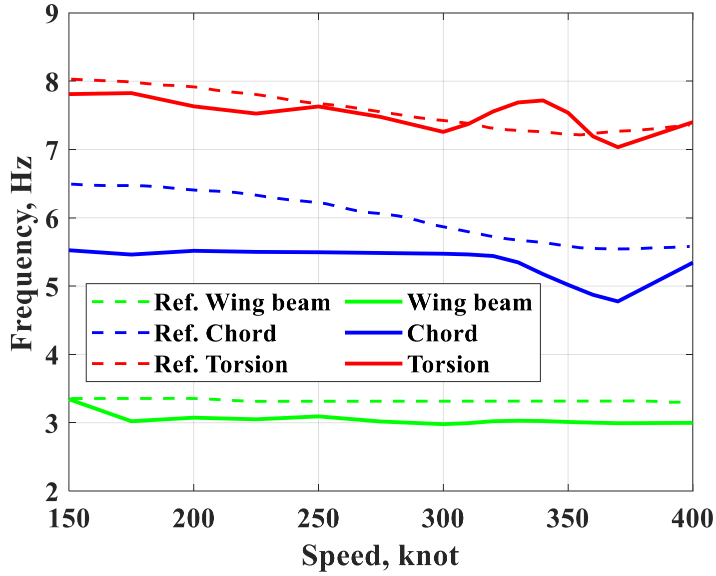

(a) Whirl-mode frequency versus airspeed

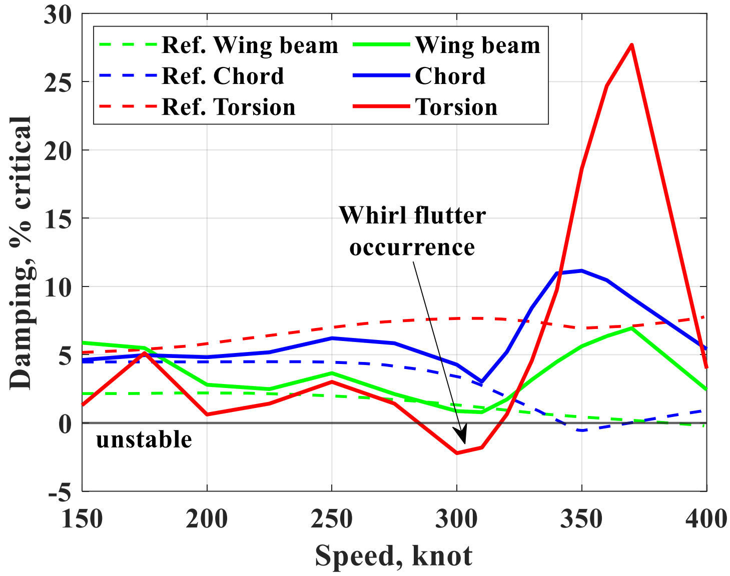

(b) Whirl-mode damping versus airspeed

Fig. 4.3 Symmetric whirl mode for Case 2 (worst case)

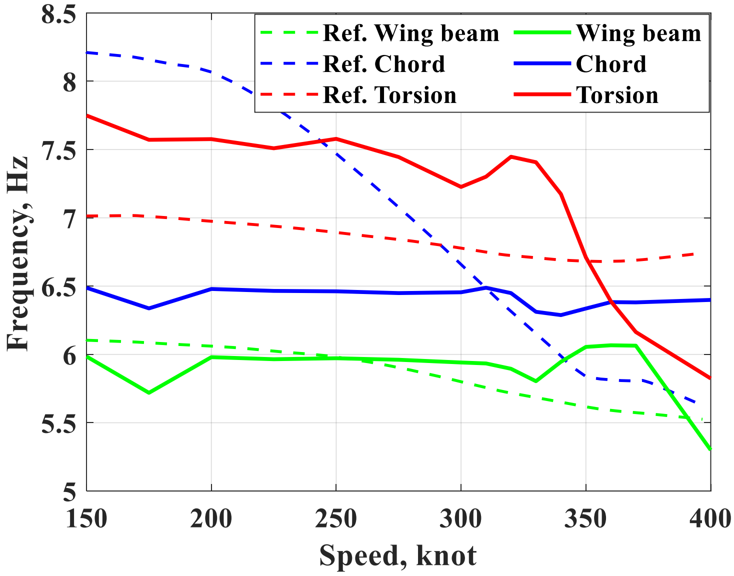

(a) Whirl-mode frequency versus airspeed

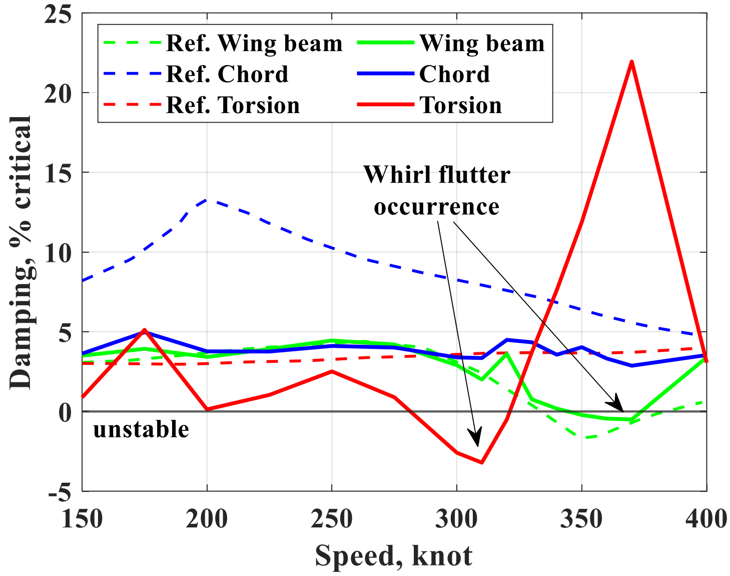

(b) Whirl-mode damping versus airspeed

Fig. 4.4 Anti-symmetric whirl mode for Case 2 (worst case)

Chapter 5

Conclusion

5.1 Conclusion

To design the improved tiltrotor engine-nacelle drive system, the mechanism investigation based on patents is conducted. XV-15 aircraft is chosen as the baseline object, and modifications are made to the engine-nacelle drive system. The drive system design is performed utilizing the gear analysis software ZAR/ROMAX, and SOLIDWORKS.

In order to obtain the sizing conditions required for the gear design, a quasi-steady transition is performed using the CAMRAD II free wake model. The analysis model is validated from the flight simulation and the experimental data in the literature. Thereafter, the required loads are derived from physics-based two-dimensional analysis using the steady components of the rotor hub.

The wing mode information necessary for the whirl flutter are obtained through mode analysis using NASTRAN. The baseline object demonstrated an exact correspondence between the frequencies and mode shapes from the reference. Based on the result, the improved drive system is applied to the baseline representation. The drive-system is attached on the wing-tip using RB2 element, considering its elasticity and contact condition. The increased weight of the drive system resulted in a 5% increase in the aircraft gross weight.

Whirl flutter analyses are conducted on the modified aircraft representation with the improved drive system using CAMRAD II. In the case of constant power, not any aeroelastic instability is observed. However, in the worst-case scenario, at a speed of 300 knots, both symmetric and anti-symmetric modes exhibit an unstable torsion mode with negative critical damping. This instability in the torsion mode is attributed to structural configuration within the engine-nacelle drive system.

5.2 Recommendation for the future work

The followings are suggested for the future tasks to approve the maturity for improved drive system design and whirl flutter analysis.

1. In the thesis, a quasi-steady transition for the rotor-hub conversion system is executed to obtain the load analysis required for the gear sizing. However, there are limitations due to the possibility of higher moments being imposed within the nacelle angle range of 0 to 30°. To derive the more accurate gear sizing condition, the pitching moment on the conversion axis over the time domain, a precise transient analysis is recommended.
2. For a more precise design of the drive system, it is recommended to apply the load condition at each gear stage. Considering the additional constraint, the gear module will decrease as the gear stage increases, allowing a reduction in the gear size. Consequently, the size of the gearbox housing will also decrease, resulting in a weight reduction in the entire drive system.

3. Improvements to whirl-mode damping can be exploited with some key parameters, such as the pitch-flap coupling (δ_3) and pitch link stiffness. $\delta 3$ is the kinematic feedback of the flapping displacement to the blade pitch motion which is a coupling between the blade flapping and pitch [13]. For positive δ_3, flapping up decreases the blade pitch which leads to lift reduction producing a change in the flapping moment that opposes the original flapping motion. Thus positive δ_3 acts as an aerodynamic spring on the flapping motion, which will be studied in no time.

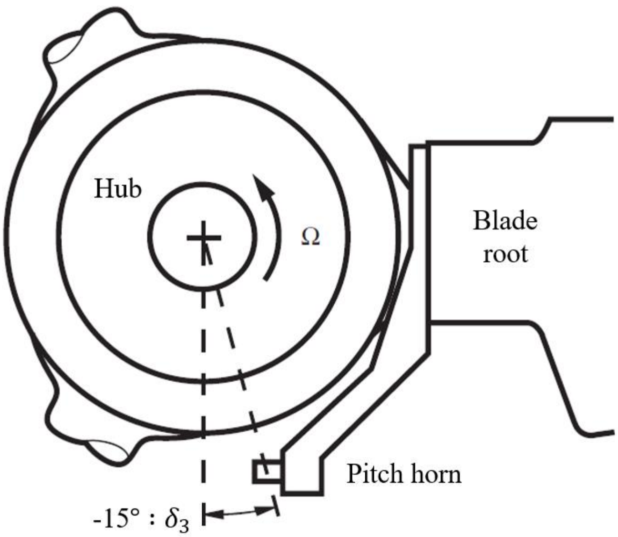

Fig. 5.5 XV-15 hub and trailing pitch horn [10]

References

[1] Maisel, M., Giulianetti, D.J. and Dugan D.C., "The History of the XV-15 Tilt Rotor Research Aircraft from Concept to Flight," NASA SP-2000-4517, February

[2] White, G., "V-22 Nacelle Conversion Actuator," Proceedings of the Institution of Mechanical Engineers, Part G: *Journal of Aerospace Engineering*," Vol. 207, (1), 1993, pp. 61-72.

[3] Kim, T., Shin, S., and Kim, T., "Analysis of tiltrotor whirl flutter in time and frequency domain," *Journal of Mechanical Science and Technology* 23, pp. 3281-3291, 2009

[4] Piatak, D. J., Kvaternik, R. G., Nixon, M. W., Langston, C. W., Singleton, J. D., Bennett, R. L. and Brown, R. K., "A Parametric Investigation of Whirl-Flutter Stability on the WRATS Tiltrotor Model," *Journal of the American Helicopter Society*, Vol. 47, (2), 2002, pp. 134-144.

[5] Muscarello, V. and Quaranta G., "Optimal Tiltrotor Blade Twist to Extend Whirl-Flutter Stability Boundaries," *AIAA SciTech 2023 Forum*,

[6] Kim, D., Lee, D., Hwang, C., "Preliminary Study on the Tiltrotor Whirl Flutter Stability," *The Korean Society for Aeronautical Space Sciences*, KSAS05-1506, 2005.

[7] Rigo, A., Muscarello, V., Masarati, P. and Quaranta, G., "Drivetrain Modeling Effects on Tiltrotor Aeroelastic Analysis," *AIAA Scitech 2019 Forum*, California, January 2019.

[8] Whittle, R., "Bell V-280 Tiltrotor Design Reflects V-22 Lessons, Army Requirements," *American Helicopter Society, JMR Tech Demo Update*, Vol. 62, (1), 2016

[9] Sidle, S., Sridharan, A., and Chopra, I., "Coupled Vibration Prediction of Rotor-Airframe-Drivetrain-Engine Dynamics," *American Helicopter Society 74th Annual Forum*, 2018, pp. 1–13.

[10] Acree, C. W., Peyran, R. J., and Johnson, W., "Rotor Design Options for Improving XV-15 Whirl-Flutter Stability Margins," NASA/TP-2004-212262, 2004.

[11] Johnson, W., "NDARC NASA Design and Analysis of Rotorcraft, Theory." Release 1.15, NASA Ames Research. 2020.

[12] Johnson, W., "NDARC — NASA Design and Analysis of Rotorcraft Validation and Demonstration," *American Helicopter Society Aeromechanics Specialists's Conference*, Jan 2010.

[13] Magee, J. P., and Alexander, H. R., "A Hingeless Rotor XV-15 Design Integration Feasibility Study Volume 1: Engineering Design Studies," NASA-CR-152310, March 1978.

[14] Hofmann, D. A., Kohler, H. K. and Munro, R. G., "Gear Technology, Module 4 Design and Stress Analysis of Spur and Helical Gears." *British Gear Association*, 1991.

[15] Pawer, P. V. and Kulkarni, P. R., "Design of Two Stage Planetary Gear Train For High Reduction Ratio," *International Journal of Research in Engineering and Technology*," eISSN2319-1163, 2015

[16] Ross, B. C., Bockmiller, D. R., McCullough, J. R. and Carlson, D. G., "Fixed Fixed Engine and Rotating Prop-rotor Arrangement for a Tiltrotor Aircraft," US9174731B2, Bell Helicopter Textron Inc., 2015.

[17] Covington, C. E., Olson, E. S., Bockmiller, D. R. and Fenny, C. A., "Rotary Pylon Conversion Actuator For Tiltrotor Aircraft," US10,106,255B2, Bell Helicopter Textron Inc., 2018

[18] Maciejczyk, A. and Zdziennicki, Z., "Design Basic of Industrial Gear Boxes Calculation and Design Case Example," Technical University of Lodz, 2007.

[19] Tran, S., Lim, J. and Bowen-Davies, G., "CFD Calculations of the XV-15 Tiltrotor During Transition," *Vertical Flight Society, Forum 75*, 2019

[20] Kumar, A. and Patil, P. P., "Modal Analysis of Heavy Vehicle Truck Transmission Gearbox Housing Made From Different Materials," *Journal of Engineering Science and Technology*, Vol. 11, (2), 2016, pp. 252-266.

[21] Kumar, G. S. and Krishnappa G. B., "Design and finite element analysis of AISI 4340 alloy steel helical gear," Materials Today: Proceedings, Vol. 65, (8), 2022, pp. 3671-3674.

[22] Staff of Bell Helicopter Company: V/STOL Tilt Rotor Research Aircraft—Volume 3: Structural Loads and Dynamics. Bell Helicopter Co. Report, No. 301-199-003, 1974.

국문초록

개선된 엔진-나셀 틸팅 메커니즘을 따른 틸트로터 항공기의 공기역학 및 공력탄성학 효과

이현재
서울대학교 대학원
항공우주공학과

틸트로터 항공기는 수직 이착륙 능력과 높은 순항속도로 기존 회전익기에 비해 장점을 가지지만, 높은 전진속도에서 날개와 로터 간의 상호작용에 의한 훨 플러터 불안정성이 발생한다. 이러한 문제를 해결하기 위하여 복수의 공력탄성학적 안정성에 대한 방법론이 시도되어왔다. 피치-플랩 커플링, 플랩핑 힌지 오프셋, 엔진/나셀의 강성과 감쇠비를 조절하는 대표적인 방법론들이 시도되어 왔으나 틸트로터 항공기에 이용된 엔진/나셀 구동부의 전체적인 구조에 의한 공력탄성학적 특성이 고려된 연구는 소수에 불과하였다.

본 논문에서는 틸트로터 항공기의 엔진/나셀 구동부 변화에 따른 틸트로터 항공기의 훨 플러터 영향성을 분석하였다. 해석의 구성은 XV-15 기종을 기반 항공기로, 해당 항공기의 엔진/나셀 구동부를 최근 새로운 틸팅 메커니즘이 적용된 V280 Valor 기종의 메커니즘으로

변경하였다. 먼저 설계 대상 기어박스를 top-down 방식으로 감속비 및 초기 형상 정보를 선정하고, 각 기어 및 구성품의 설계에 필요한 하중 해석을 수행한다. CAMRAD II 해석 프로그램의 자유 후류 모델을 이용한 로터의 준정상 천이해석을 수행하였고, 도출된 결과를 기반으로 한 물리적 접근을 통해 기어 설계에 필요한 하중을 추출하였다. 이후 기어 및 드라이브 시스템의 사이징 및 모델링을 수행하고, 전체 엔진-나셀 시스템은 접촉 조건이 고려된 유연체로서 기반 항공기의 날개 끝단 지점에 강체 요소로 부착되었다. NASTRAN 프로그램을 이용한 고유 주파수 및 모드를 비교하고, CAMRAD II 의 플러터 해석기능을 이용하여, 항공기 트림해석을 수행하였다. 해당 결과를 바탕으로 개선된 구동부가 적용된 항공기 주 날개의 임계 감쇠비와 주파수를 통해 훨 플러터 영향성을 파악하였다.

주제어: 틸트로터, 엔진-나셀 틸팅 메커니즘, 훨플러터, 기어박스 설계

학번: 2021-23313